IEEE Open Journal of
Industry Applications

Received 23 May 2021; revised 21 July 2021; accepted 26 July 2021. Date of publication 30 July 2021;
date of current version 16 August 2021. The review of this paper was arranged by Associate Editor Mauro Di Nardo.

Digital Object Identifier 10.1109/OJIA.2021.3100867

Three-Dimensional Analytical Modeling of an Eddy-Current-Based Non-Contact Speed Sensor

ARDA TÜYSÜZ [1,2], TIBOR STOLZ [1], ANNETTE MUETZE [3] (Fellow, IEEE), MICHAEL FLANKL [1] (Student Member, IEEE), SPASOJE MIRIĆ [1] (Student Member, IEEE), AND JOHANN W. KOLAR [1] (Fellow, IEEE)

[1]Power Electronic Systems Laboratory, ETH Zurich, 8092 Zurich, Switzerland
[2]ABB Corporate Research Center, 68526 Ladenburg, Germany
[3]Electric Drives and Machines Institute, Graz University of Technology, 8010 Graz, Austria

CORRESPONDING AUTHOR: S. MIRIĆ (E-mail: miric@lem.ee.ethz.ch)

This work was supported by Nabtesco Corp., Japan, for the research on Advanced Mechatronic Systems at the Power Electronic Systems Laboratory, ETH Zurich.

ABSTRACT This paper presents a computationally efficient, three-dimensional electromagnetic model for eddy-current-based speed sensors featuring an injection coil, two or more pick-up coils and a magnetic yoke. The superposition of incident and reflected fields, which was adopted in previous works, is replaced by a direct formulation; and Maxwell's equations are solved for the magnetic flux density vector, rather than involving a higher-order vector potential. The injected current is accounted for in the boundary conditions, and special attention is given to the modeling of the in-plane spreading of the coils by deriving coil-linkage functions. The magnetic field and eddy current distributions in the whole problem space is obtained by algebraically solving a 12-by-12 linear equation system. Results of the model are compared to experimental results from earlier publications for verifying the validity of the models. Even though derived primarily with the eddy-current-based speed sensing application in mind, the analysis presented in this paper can potentially contribute to various other eddy-current-based applications such as non-destructive testing, where probes with a magnetic yoke are utilized.

INDEX TERMS Analytical modeling, eddy-current modeling, fourier transform, speed sensing.

I. INTRODUCTION

In applications where the rotational or translational speed of a smooth surface featuring no mechanical, optical or magnetic saliency is to be measured, and the mechanical contact of the speed sensor and the moving surface is to be avoided, conventional contactless speed measurement methods such as variable-reluctance or optical sensors are not applicable.

The eddy-current-based, non-contact speed sensor depicted in Fig. 1 provides a viable speed sensing method in such cases. This sensor comprises an injection coil and two pick-up coils arranged in a plane that is parallel to the movement of the body whose speed is to be measured. Additionally, a magnetic yoke spans over all three coils. If an AC current with a constant amplitude flows in the injection coil, eddy currents are induced in the moving body, which is required to have a non-zero electrical conductivity. The distribution of these eddy currents is symmetrical in case the conductive body is at standstill. Consequently, the voltage induced in the two pick-up coils is identical. However, when the body is in motion ($v_x \neq 0$ and/or $v_z \neq 0$) the distribution of the eddy currents is skewed proportionally to the speed. Hence, in the example depicted in Fig. 1, different voltages are induced in the two pick-up coils when $v_x \neq 0$. The measurement of this voltage difference (e.g. by anti-series connection of the pick-up coils) yields an AC voltage, whose amplitude and phase contain the speed information. The speed sensor shown in Fig. 1 is used as an example throughout the paper for the 3D analytic model derivation and later as a prototype to verify the model results. It should be noted that another types of eddy current based speed sensors are possible, e.g. [1] where

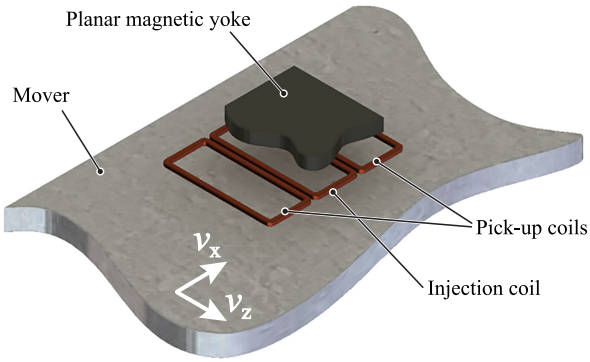

FIGURE 1. The analyzed eddy-current-based non-contact speed sensor comprising a planar magnetic yoke, an injection coil and two pick-up coils. The yoke is displayed as a cutaway view for better visualization of the coils.

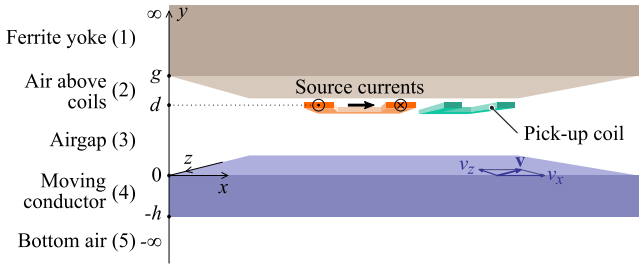

FIGURE 2. Problem geometry for the analytical eddy current model. A vertically layered material setup with infinite horizontal extension is assumed.

a Hall-element together with a permanent magnet is used used to deduce the speed of a conductive surface.

Eddy current modeling is not a novel topic (cf. [2], [3]) and extensive work on the analytical modeling of similar sensor arrangements with circular injection and pick-up coils ([4], [5]), as well as a rectangular injection coil of arbitrary orientation towards the moving body ([6]–[8]) has been presented in literature. However, these works only deal with the modeling of the coils and the moving body surrounded by air, i.e, they cannot be used to model sensors where a magnetic yoke is utilized. A magnetic yoke, on the other hand, increases the sensor's signal-to-noise ratio and/or decreases its power consumption by intensifying the air gap flux density for the same injected current. Moreover, it shields the sensor magnetically and avoids a potential magnetic interference of the sensor with its environment. Therefore, two-dimensional (2-D) time-transient finite element method (FEM) is used in [9] to optimize the geometry of an eddy-current-based speed sensor featuring a magnetic yoke. Even though it offers a flexible and easy-to-set-up modeling environment, such FEM analysis is computationally very demanding, which limits its use in modeling practical systems with a large air-gap-to-skin-depth ratio. Similarly, in [10], a finite-difference method is used to model a sensor with rectangular excitation and pick-up coils with a magnetic yoke.

Moreover, while 2-D electromagnetic models can be used to design speed sensors that can measure a one-dimensional speed (either $v_x = 0$ or $v_z = 0$, see Fig. 1), three-dimensional (3-D) models are required for modeling speed sensors that can measure a 2-D, in-plane speed (both $v_x \neq 0$ and $v_z \neq 0$, see Fig. 1). Optimization of such sensors can be impractical with 3-D FEM due to the long calculation times, even using the state-of-the-art computers and commercial software packages.

Therefore, this paper presents a computationally efficient, 3-D electromagnetic modeling approach for eddy-current-based speed sensors featuring a magnetic yoke. The superposition of incident and reflected fields, which was adopted in the above-mentioned works, is replaced by a direct formulation with boundary currents, and Maxwell's equations are solved directly for the magnetic flux density vector, rather than involving a higher-order vector potential. The injected current is accounted for in the boundary conditions, and the in-plane spreading of the coils is represented in the derived coil-linkage functions. The magnetic field and eddy current distribution in the whole problem space is obtained by algebraically solving a 12-by-12 linear equation system, and finally the induced voltages in all coils are evaluated by a symbolic integration of the magnetic flux density in the coil region.

Even though derived primarily with the eddy-current-based speed sensing application in mind, the analysis presented in this paper can potentially contribute to various other eddy-current-based applications such as Lorentz force velocimetry [11], or non-destructive testing, where probes comprising coils and a magnetic yoke are utilized [12]–[14].

II. ANALYTICAL MODELING

A. PROBLEM DEFINITION AND MODEL LIMITATIONS

The geometry assumed for the analytic model is illustrated in Fig. 2. A planar soft-magnetic yoke is mounted with a certain air gap g above a conductive plate, which is horizontally moving relative to the yoke. Both pieces are modeled with infinite length in z-direction and width in x-direction. This hypothesis of infinite size in z and x directions is well justified, as in practical applications the sensor size is much smaller that the moving conductor size and the magnetic yoke always covers the coils, which is the region of relevant field change. Finally, in Sec. IV this hypothesis is verified by measurement results. The conductive plate has a finite thickness, whereas the yoke extends infinitely towards the top in y-direction. The electrical conductivity of the yoke material is assumed to be zero.

An arbitrary number of rectangular coils are placed between the yoke and the moving plate, of which only one carries a sinusoidal current of given amplitude. The voltages (amplitude and phase) are to be determined for all those coils. In order to keep the mathematical derivation effort to a minimum, the coils are modeled as sheets in the $x - z$ plane, located at a given height ($y = d$ in Fig. 2).

The model is limited to linear isotropic materials (i. e. $\mu_r = \text{const}$, $\sigma = \text{const}$). With the given restrictions of geometry, such as material boundaries only occurring as parallel infinite planes, and the exciting current flowing as a planar

sheet of zero thickness, a mathematically exact solution can be formulated. However, as an effect of the employed double Fourier transform, a numerically approximated double integration is required for all results; most notably, the magnetic field and eddy current distributions will become periodic in typical implementations (superposition of finite number of sinusoids).

B. CONSTITUTIVE EQUATIONS AND GENERAL SOLUTIONS

The eddy current model is derived from an adapted set of Maxwell's equations [4], [15]–[17], where the conductor movement is incorporated as a modification of the electric field. As a result from Lorentz transformation, we have in a coordinate system moving with the plate

$$\mathbf{E}' = \mathbf{E} + \mathbf{v} \times \mathbf{B}. \tag{1}$$

Inserting this in Ohm's law $\mathbf{J} = \sigma \mathbf{E}$, we obtain

$$\operatorname{rot} \mathbf{H} = \mathbf{J} = \sigma \left(\mathbf{E} + \mathbf{v} \times \mathbf{B}\right) \tag{2a}$$

$$\operatorname{rot} \mathbf{E} = -\frac{\partial}{\partial t}\mathbf{B} \tag{2b}$$

$$\operatorname{div} \mathbf{B} = 0. \tag{2c}$$

As usually done in quasistatic magnetic field analysis, the displacement currents $\frac{\partial}{\partial t}\mathbf{D}$ are neglected in (2a).

In the moving conductive plate (region 4, see Fig. 2), taking $\mathbf{B} = \mu \mathbf{H}$ and eliminating $\mathbf{E}$ leads to

$$\operatorname{rot} \operatorname{rot} \mathbf{B} = \mu\sigma \left(-\frac{\partial}{\partial t}\mathbf{B} + \operatorname{rot}(\mathbf{v} \times \mathbf{B})\right) \tag{3a}$$

$$\Rightarrow \quad \Delta \mathbf{B} = \mu\sigma \left(\frac{\partial}{\partial t}\mathbf{B} + (\mathbf{v} \bullet \nabla)\mathbf{B}\right). \tag{3b}$$

All B-field components are decoupled, such that a separate scalar equation holds for each component $i \in \{x, y, z\}$

$$\left(\frac{\partial^2}{\partial x^2} + \frac{\partial^2}{\partial y^2} + \frac{\partial^2}{\partial z^2}\right) B_i = \mu\sigma \left(\frac{\partial}{\partial t} + v_x \frac{\partial}{\partial x} + v_y \frac{\partial}{\partial y} + v_z \frac{\partial}{\partial z}\right) B_i. \tag{3c}$$

In all non-conductive regions (yoke and air), from $\sigma = 0$ follows $\mathbf{J} = 0 \Rightarrow \operatorname{rot} \mathbf{H} = 0$. Therefore, a magnetic scalar potential ϕ can be defined such that $\mathbf{H} = -\operatorname{grad} \phi$, for which a Laplace equation holds

$$\Delta\phi = \left(\frac{\partial^2}{\partial x^2} + \frac{\partial^2}{\partial y^2} + \frac{\partial^2}{\partial z^2}\right) \phi = 0. \tag{4}$$

The constitutive equations (4) and (4) are solved in the frequency domain. As the injected current and hence all fields are sinusoidal with angular frequency ω, these can be represented by phasors $\underline{B}$

$$B(x, y, z, t) = \operatorname{Re}\left\{\underline{B}(x, y, z)\, \mathrm{e}^{\mathrm{i}\omega t}\right\}. \tag{5a}$$

Further, we introduce the double Fourier transform $\mathcal{B}(\xi, y, \zeta)$ of $\underline{B}(x, y, z)$, such that

$$\underline{B}(x, y, z) = \frac{1}{(2\pi)^2} \int_{-\infty}^{\infty} \int_{-\infty}^{\infty} \mathcal{B}(\xi, y, \zeta)\, \mathrm{e}^{\mathrm{i}\xi x} \mathrm{e}^{\mathrm{i}\zeta z}\, \mathrm{d}\xi\, \mathrm{d}\zeta. \tag{5b}$$

This replaces partial derivatives in t, x, z by factors $\mathrm{i}\omega, \mathrm{i}\xi, \mathrm{i}\zeta$. The remaining differential equation in y is then easily solved, and the general solution in the conductive region

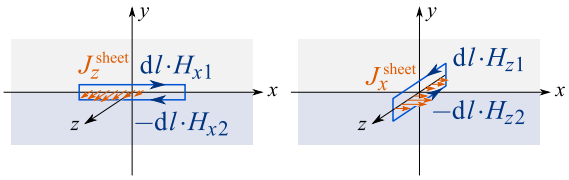

FIGURE 3. Integration contours for continuity conditions with a boundary current sheet.

follows

$$\beta := \sqrt{\xi^2 + \zeta^2 + \mathrm{i}\mu\sigma\,(\omega + \xi v_x + \zeta v_z)} \tag{6a}$$

$$\mathcal{B}_{4x} = C_{4x}\, \mathrm{e}^{\beta y} + D_{4x}\, \mathrm{e}^{-\beta y} \tag{6b}$$

$$\mathcal{B}_{4y} = C_{4y}\, \mathrm{e}^{\beta y} + D_{4y}\, \mathrm{e}^{-\beta y} \tag{6c}$$

$$\mathcal{B}_{4z} = C_{4z}\, \mathrm{e}^{\beta y} + D_{4z}\, \mathrm{e}^{-\beta y}. \tag{6d}$$

In the non-conductive regions $n \in \{1, 2, 3, 5\}$, the same procedure followed by evaluation of $\mathbf{B} = -\mu \operatorname{grad} \phi$ gives

$$\alpha := \sqrt{\xi^2 + \zeta^2} \tag{7a}$$

$$\mathcal{B}_{nx} = \mathrm{i}\xi\, C_n\, \mathrm{e}^{\alpha y} + \mathrm{i}\xi\, D_n\, \mathrm{e}^{-\alpha y} \tag{7b}$$

$$\mathcal{B}_{ny} = \alpha\, C_n\, \mathrm{e}^{\alpha y} - \alpha\, D_n\, \mathrm{e}^{-\alpha y} \tag{7c}$$

$$\mathcal{B}_{nz} = \mathrm{i}\zeta\, C_n\, \mathrm{e}^{\alpha y} + \mathrm{i}\zeta\, D_n\, \mathrm{e}^{-\alpha y}. \tag{7d}$$

The decay factors β and α and all (still unknown) amplitude coefficients C and D are functions of the spatial Fourier frequencies ξ, ζ. The terms $C_1 \mathrm{e}^{\alpha y}$ and $D_5 \mathrm{e}^{-\alpha y}$ are discarded, since they would lead to infinitely growing fields with increasing vertical distance $y \to \pm\infty$.

C. BOUNDARY CONDITIONS AND SPECIFIC SOLUTION

At the region interface planes, the usual boundary conditions apply, i. e. continuity of normal B_y and tangential H_x, H_z. The boundary between the air regions 2 and 3 requires special attention, because it contains the injection coil, modeled as a planar current sheet of zero height. Evaluating Ampère's circuital law $\oint \mathbf{H} \bullet \mathrm{d}\mathbf{l} = \iint \mathbf{J} \bullet \mathrm{d}\mathbf{A}$ on very small paths across the boundary as shown in Fig. 3, we find

$$H_{x,\text{top}} = H_{x,\text{bottom}} - J_{z,\text{sheet}} \tag{8a}$$

$$H_{z,\text{top}} = H_{z,\text{bottom}} + J_{x,\text{sheet}}. \tag{8b}$$

In terms of the general solutions in Fourier domain (6a–7d), the boundary conditions give the following equations between the amplitude coefficients:

$$D_1\, \mathrm{e}^{-\alpha g} - C_2\, \mu_{r1}\, \mathrm{e}^{\alpha g} - D_2\, \mu_{r1}\, \mathrm{e}^{-\alpha g} = 0 \tag{9a}$$

$$-D_1\, \mathrm{e}^{-\alpha g} - C_2\, \mathrm{e}^{\alpha g} + D_2\, \mathrm{e}^{-\alpha g} = 0 \tag{9b}$$

$$C_2\, \mathrm{e}^{\alpha d} + D_2\, \mathrm{e}^{-\alpha d} - C_3\, \mathrm{e}^{\alpha d} - D_3\, \mathrm{e}^{-\alpha d} = -\mu_0 \frac{\mathcal{J}_z}{\mathrm{i}\xi} \tag{9c}$$

$$C_2\, \mathrm{e}^{\alpha d} + D_2\, \mathrm{e}^{-\alpha d} - C_3\, \mathrm{e}^{\alpha d} - D_3\, \mathrm{e}^{-\alpha d} = \mu_0 \frac{\mathcal{J}_x}{\mathrm{i}\zeta} \tag{9d}$$

$$C_2\,\mathrm{e}^{\alpha d} - D_2\,\mathrm{e}^{-\alpha d} - C_3\,\mathrm{e}^{\alpha d} + D_3\,\mathrm{e}^{-\alpha d} = 0 \tag{9e}$$

$$(C_3 + D_3)\,\mu_{r4}\,\mathrm{i}\xi - C_{4x} - D_{4x} = 0 \tag{9f}$$

$$C_3\,\alpha - D_3\,\alpha - C_{4y} - D_{4y} = 0 \tag{9g}$$

$$(C_3 + D_3)\,\mu_{r4}\,\mathrm{i}\zeta - C_{4z} - D_{4z} = 0 \tag{9h}$$

$$C_{4x}\,\mathrm{e}^{-\beta h} + D_{4x}\,\mathrm{e}^{\beta h} - C_5\,\mu_{r4}\,\mathrm{i}\xi\,\mathrm{e}^{-\alpha h} = 0 \tag{9i}$$

$$C_{4y}\,\mathrm{e}^{-\beta h} + D_{4y}\,\mathrm{e}^{\beta h} - C_5\,\alpha\,\mathrm{e}^{-\alpha h} = 0 \tag{9j}$$

$$C_{4z}\,\mathrm{e}^{-\beta h} + D_{4z}\,\mathrm{e}^{\beta h} - C_5\,\mu_{r4}\,\mathrm{i}\zeta\,\mathrm{e}^{-\alpha h} = 0, \tag{9k}$$

where g, d and h describe the geometry according to Fig. 2. The general solution for the moving conductor does not fully utilize Gauss's law $\operatorname{div}\mathbf{B} = 0$. This manifests in the situation that the C and D functions cannot be determined from the system of boundary conditions, since there are not enough equations. For that reason, differential form of the Gauss's law needs to be stated as an additional equation, which leads to

$$C_2\,\mathrm{e}^{\alpha d} + D_2\,\mathrm{e}^{-\alpha d} - C_3\,\mathrm{e}^{\alpha d} - D_3\,\mathrm{e}^{-\alpha d} C_{4x}\,\mathrm{i}\xi + C_{4y}\,\beta + C_{4z}\,\mathrm{i}\zeta = 0 \tag{9l}$$

$$D_{4x}\,\mathrm{i}\xi - D_{4y}\,\beta + D_{4z}\,\mathrm{i}\zeta = 0. - \mu_0 \frac{\mathcal{J}_z}{\mathrm{i}\xi} \tag{9m}$$

The equations (9c) and (9d) have the same left-hand side, therefore:

$$-\mu_0 \frac{\mathcal{J}_z}{\mathrm{i}\xi} = \mu_0 \frac{\mathcal{J}_x}{\mathrm{i}\zeta} \quad \Longrightarrow \quad \mathrm{i}\xi\,\mathcal{J}_x + \mathrm{i}\zeta\,\mathcal{J}_z = 0, \tag{10}$$

which is the Fourier transform of $\operatorname{div}\mathbf{J}_{\text{sheet}} = 0$, as the sheet current density has no J_y component.

The remaining system of 12 independent equations yields the following solution for the amplitude coefficients:

$$\boldsymbol{Ccom} := (\beta + \alpha\mu_{r4})^2 - \mathrm{e}^{-2\beta h}(\beta - \alpha\mu_{r4})^2 \tag{11a}$$

$$\boldsymbol{Dcom} := \left(1 - \mathrm{e}^{-2\beta h}\right)\left(\beta^2 - \alpha^2\mu_{r4}^2\right) \tag{11b}$$

$$\boldsymbol{comm} := \boldsymbol{Ccom} - \mathrm{e}^{-2\alpha d}\boldsymbol{Dcom} \tag{11c}$$

$$\boldsymbol{mre} := (\mu_{r1} + 1) + (\mu_{r1} - 1)\,\mathrm{e}^{-2\alpha(g-d)} \tag{11d}$$

$$\boldsymbol{denom} := (\mu_{r1} + 1)\boldsymbol{Ccom} + \mathrm{e}^{-2\alpha g}(\mu_{r1} - 1)\boldsymbol{Dcom} \tag{11e}$$

$$D_1\mathrm{e}^{-\alpha d} = -\mu_{r1} \cdot \boldsymbol{comm}\ \frac{\mu_0\mathcal{J}_z/\mathrm{i}\xi}{\boldsymbol{denom}} \tag{11f}$$

$$C_2\mathrm{e}^{\alpha g} = \tfrac{1}{2}\,\mathrm{e}^{-\alpha(g-d)}\,(\mu_{r1} - 1) \cdot \boldsymbol{comm}\ \frac{\mu_0\mathcal{J}_z/\mathrm{i}\xi}{\boldsymbol{denom}} \tag{11g}$$

$$D_2\mathrm{e}^{-\alpha d} = -\tfrac{1}{2}\,(\mu_{r1} + 1) \cdot \boldsymbol{comm}\ \frac{\mu_0\mathcal{J}_z/\mathrm{i}\xi}{\boldsymbol{denom}} \tag{11h}$$

$$C_3\mathrm{e}^{\alpha d} = \tfrac{1}{2}\,\boldsymbol{mre} \cdot \boldsymbol{Ccom}\ \frac{\mu_0\mathcal{J}_z/\mathrm{i}\xi}{\boldsymbol{denom}} \tag{11i}$$

$$D_3 = \tfrac{1}{2}\,\mathrm{e}^{-\alpha d}\,\boldsymbol{mre} \cdot \boldsymbol{Dcom}\ \frac{\mu_0\mathcal{J}_z/\mathrm{i}\xi}{\boldsymbol{denom}} \tag{11j}$$

$$C_4 := \mathrm{e}^{-\alpha d}\,\mu_{r4}\,\boldsymbol{mre}\,(\beta + \alpha\mu_{r4})\ \frac{\mu_0\mathcal{J}_z/\mathrm{i}\xi}{\boldsymbol{denom}} \tag{11k}$$

$$D_4\mathrm{e}^{\beta h} := \mathrm{e}^{-\alpha d - \beta h}\,\mu_{r4}\,\boldsymbol{mre}\,(\beta - \alpha\mu_{r4})\ \frac{\mu_0\mathcal{J}_z/\mathrm{i}\xi}{\boldsymbol{denom}} \tag{11l}$$

$$C_5\mathrm{e}^{-\alpha h} = \mathrm{e}^{-\alpha d - \beta h}\,\boldsymbol{mre} \cdot 2\alpha\mu_{r4}\beta\ \frac{\mu_0\mathcal{J}_z/\mathrm{i}\xi}{\boldsymbol{denom}} \tag{11m}$$

$$\left[C_{4x}, C_{4y}, D_{4z}\right] = \left[\mathrm{i}\xi\,\beta, \alpha^2, \mathrm{i}\zeta\,\beta\right] \cdot C_4 \tag{11n}$$

$$\left[D_{4x}, D_{4y}, D_{4z}\right] \cdot \mathrm{e}^{\beta h} = \left[\mathrm{i}\xi\,\beta, -\alpha^2, \mathrm{i}\zeta\,\beta\right] \cdot D_4\mathrm{e}^{\beta h} \tag{11o}$$

Exponential factors are deliberately placed on the left-hand side to improve numerical calculations: When e. g. $C_2 \cdot \mathrm{e}^{\alpha y}$ is implemented as $C_2\mathrm{e}^{\alpha g} \cdot \mathrm{e}^{-\alpha(g-y)}$, the magnitude of the y-dependent term never exceeds 1 inside region 2, but equals 1 at $y = g$. This eliminates any $\frac{0}{0}$ and $\frac{\infty}{\infty}$ problems with large exponents.

D. EDDY CURRENT DISTRIBUTION

The eddy currents in the moving conductive plate are found by reconsidering Ampère's circuital law, $\mathbf{J} = \operatorname{rot}\mathbf{H} = \operatorname{rot}\mathbf{B}/\mu$ with $\mu := \mu_0\mu_{r4}$. Coordinate-wise evaluation in Fourier domain gives

$$\begin{aligned}\mathcal{J}_{4x} &= \tfrac{1}{\mu}\left(\tfrac{\partial}{\partial y}\mathcal{B}_{4z} - \mathrm{i}\zeta\,\mathcal{B}_{4y}\right)\\ &= \underbrace{\tfrac{1}{\mu}\left(\beta C_{4z} - \mathrm{i}\zeta C_{4y}\right)}_{C_{J4x}}\mathrm{e}^{\beta y} + \underbrace{\tfrac{1}{\mu}\left(-\beta D_{4z} - \mathrm{i}\zeta D_{4y}\right)}_{D_{J4x}}\mathrm{e}^{-\beta y}\end{aligned} \tag{12a}$$

$$\begin{aligned}\mathcal{J}_{4y} &= \tfrac{1}{\mu}\left(\mathrm{i}\zeta\,\mathcal{B}_{4x} - \mathrm{i}\xi\,\mathcal{B}_{4z}\right)\\ &= \underbrace{\tfrac{1}{\mu}\left(\mathrm{i}\zeta\,C_{4x} - \mathrm{i}\xi\,C_{4z}\right)}_{0}\mathrm{e}^{\beta y} + \underbrace{\tfrac{1}{\mu}\left(\mathrm{i}\zeta\,D_{4x} - \mathrm{i}\xi\,D_{4z}\right)}_{0}\mathrm{e}^{-\beta y}\end{aligned} \tag{12b}$$

$$\begin{aligned}\mathcal{J}_{4z} &= \tfrac{1}{\mu}\left(\mathrm{i}\xi\,\mathcal{B}_{4y} - \tfrac{\partial}{\partial y}\mathcal{B}_{4x}\right)\\ &= \underbrace{\tfrac{1}{\mu}\left(\mathrm{i}\xi\,C_{4y} - \beta\,C_{4x}\right)}_{C_{J4z}}\mathrm{e}^{\beta y} + \underbrace{\tfrac{1}{\mu}\left(\mathrm{i}\xi\,D_{4y} + \beta\,D_{4x}\right)}_{D_{J4z}}\mathrm{e}^{-\beta y}.\end{aligned} \tag{12c}$$

We notice that the eddy currents do not have a y-direction component. The remaining amplitude coefficients are formulated as:

$$C_{J4} := \mathrm{e}^{-\alpha d}\,\boldsymbol{mre}\,(\beta + \alpha\mu_{r4})\ \frac{\mathcal{J}_z/\mathrm{i}\xi}{\boldsymbol{denom}} \tag{13a}$$

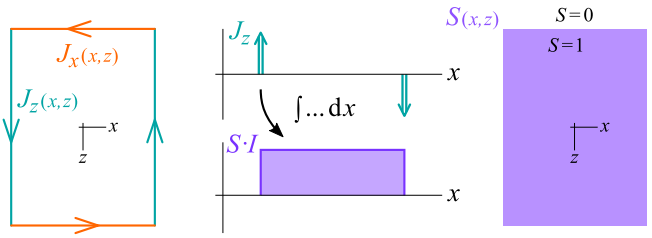

FIGURE 4. Rectangular one-turn filament coil: Integration of sheet current density, as required by the field solution, gives a box distribution (linkage function).

$$D_{J4}\mathrm{e}^{\beta h} := \mathrm{e}^{-\alpha d-\beta h}\,\boldsymbol{mre}\,(\beta-\alpha\mu_{r4})\,\frac{\mathcal{J}_z/\mathrm{i}\xi}{\boldsymbol{denom}} \tag{13b}$$

$$\left[C_{J4x}, C_{J4z}\right] = [\mathrm{i}\zeta, -\mathrm{i}\xi]\cdot(\beta^2-\alpha^2)\,C_{J4} \tag{13c}$$

$$\left[D_{J4x}, D_{J4z}\right]\cdot\mathrm{e}^{\beta h} = [\mathrm{i}\zeta, -\mathrm{i}\xi]\cdot(\beta^2-\alpha^2)\,D_{J4}\mathrm{e}^{\beta h}. \tag{13d}$$

E. COIL LINKAGE FUNCTIONS

To define the source current density $\mathcal{J}_x, \mathcal{J}_z$ of the injection coil, which produces a 2-D current sheet at $y = d$, we first consider one rectangular filament turn, as shown in Fig. 4.

For an ideally thin wire, the full current flows through a single point, such that J_x, J_z (current per cross-sectional width) must be modeled with Dirac-delta distributions. However, the field solutions (11a) actually depend on $\mathcal{J}_z/\mathrm{i}\xi$, which is the Fourier transform of the integral $\int J_z\,\mathrm{d}x$. Integration turns the delta peaks into step functions, and we find according to Fig. 4:

$$\mathcal{J}_z/\mathrm{i}\xi \;\widehat{=}\; \underline{I}\cdot S_{\mathrm{fil}}(x,z) := \underline{I}\cdot\begin{cases}1 & (x,z)\text{ inside rectangle}\\ 0 & \text{else}\end{cases} \tag{14}$$

The source term is thus the product of the injected current phasor $\underline{I}$ and a *linkage function* $S(x, z)$, which counts how many turns encircle each point. Its Fourier transform is given by two *sinc* functions:

$$\mathcal{S}_{\mathrm{fil}}(\xi,\zeta) = \underbrace{\frac{2\sin\left(\xi\frac{x_s}{2}\right)}{\xi}}_{=x_s \text{ for } \xi=0}\cdot\underbrace{\frac{2\sin\left(\zeta\frac{z_s}{2}\right)}{\zeta}}_{=z_s \text{ for } \zeta=0} \tag{15}$$

This assumes a coil centered at the origin ($x_c = 0, z_c = 0$) and having a total size of $x_s \cdot z_s$ (see Fig. 5(a)).

For a more realistic simulation of multi-turn coils, the technique of superposition of filament solutions (by means of an integral) is widely used [4]–[7], [18]. Due to the addition of a yoke, which complicates the field solution's dependence on the coil location d, a vertical integration over d is not performed in this work. However, this does not significantly hinder the applicability of the model, since a small coil height is desirable for maintaining a small air gap in practical designs.

With all turns located at $y = d$, it is easier (but mathematically equivalent) to sum up the current densities – i. e. linkage functions – of all turns, instead of the complete field solutions.

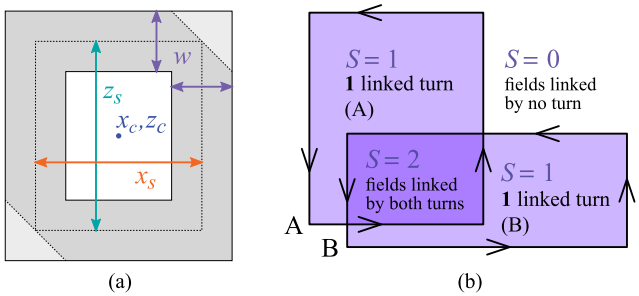

FIGURE 5. (a) Dimension parameters of a multi-turn coil. (b) Linkage function for a coil with two filament turns A and B.

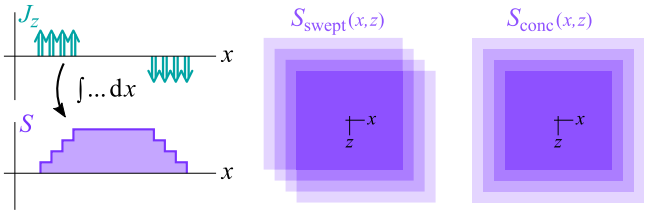

FIGURE 6. Linkage functions for rectangular multi-turn coils: Swept-rectangle approximation and concentric version.

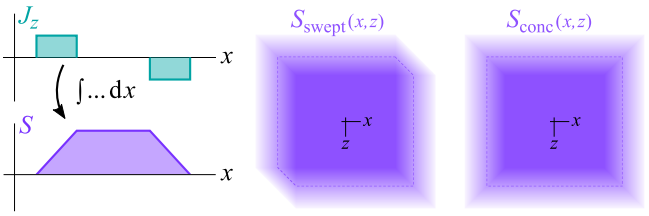

FIGURE 7. Linkage functions with many individual filament turns merged into a continuous current sheet. Formulas are given for this case only.

The total linkage function $S(x, z)$ then takes values from 0 to N (number of turns). An example with two turns, which emphasizes the geometric interpretation, is shown in Fig. 5(b).

In the Fourier domain, individual rectangular filament turns (center x_c, z_c, size $x_s \cdot z_s$) are combined using (15) and the Fourier shift property

$$\mathcal{S}_{\mathrm{combi}} = \sum_{n=1}^{N}\mathcal{S}_{\mathrm{fil}\,[x_s(n),z_s(n)]}\cdot\mathrm{e}^{-\mathrm{i}\xi x_c(n)-\mathrm{i}\zeta z_c(n)}. \tag{16}$$

In the simplest case, x_s and z_s are the same for each turn, and the center is swept in 45° diagonal direction. This already produces a good approximation to a flat multi-turn coil, as shown in Fig. 6. The formula is simplified if a continuum (Fig. 7) is considered instead of separate wires, such that the sum becomes an integral:

$$\mathcal{S}_{\mathrm{swept}} = N\cdot\mathcal{S}_{\mathrm{fil}}\cdot\int_{-w/2}^{w/2}\mathrm{e}^{-\mathrm{i}\,(\xi+\zeta)\,p}\cdot\frac{1}{w}\,\mathrm{d}p. \tag{17}$$

Here, the limit of $\mathcal{S}/N$ (range 0 to 1) for $N \to \infty$ filaments was derived first as a Riemann integral, then the original finite number of turns N was restored.

The integral in (17) evaluates to a third *sinc* term

$$\mathcal{S}_{\text{swept}}(\xi,\zeta) = N \cdot \underbrace{\frac{2\sin\left(\xi\frac{x_s}{2}\right)}{\xi}}_{=x_s \text{ for } \xi=0} \cdot \underbrace{\frac{2\sin\left(\zeta\frac{z_s}{2}\right)}{\zeta}}_{=z_s \text{ for } \zeta=0} \cdot \underbrace{\frac{2\sin\left([\xi+\zeta]\frac{w}{2}\right)}{[\xi+\zeta]}}_{=1 \text{ for } \xi+\zeta=0} \tag{18}$$

The dimensions x_s, z_s, w are defined in Fig. 5(a).

Alternatively, a coil may be built from filaments with the same geometric center but different sizes [6], [7], [18], [19]. In analogy to (17), the integral over the size variation p is given as

$$\mathcal{S}_{\text{conc}} = N \int_{-w/2}^{w/2} \frac{2\sin\left(\xi[\frac{x_s}{2}+p]\right)}{\xi} \frac{2\sin\left(\zeta[\frac{z_s}{2}+p]\right)}{\zeta} \cdot \frac{1}{w}\,\mathrm{d}p. \tag{19}$$

After mathematical treatment, this gives the result (for dimensions x_s, z_s, w see Fig. 5(a))

$$\begin{aligned}\frac{1}{N}\mathcal{S}_{\text{conc}}(\xi,\zeta) = &-4\frac{\cos\left(\xi\frac{x_s}{2}+\zeta\frac{z_s}{2}\right)}{\xi\cdot\zeta} \cdot \overbrace{\frac{\sin\left([\xi+\zeta]\frac{w}{2}\right)}{[\xi+\zeta]w}}^{=1 \text{ for } \xi+\zeta=0} \\ &+4\frac{\cos\left(\xi\frac{x_s}{2}-\zeta\frac{z_s}{2}\right)}{\xi\cdot\zeta} \cdot \underbrace{\frac{\sin\left([\xi-\zeta]\frac{w}{2}\right)}{[\xi-\zeta]w}}_{=1 \text{ for } \xi-\zeta=0}.\end{aligned} \tag{20a}$$

For numerical evaluation, more limit cases must be provided by manipulation of (20 a):

$$\begin{aligned}\frac{1}{N}\mathcal{S}_{\text{conc}}(0,\zeta) = &-4\frac{\cos\left(\zeta\frac{z_s}{2}\right)\cos\left(\zeta\frac{w}{2}\right)}{\zeta^2} + 4\frac{\sin\left(\zeta\frac{z_s}{2}\right)\sin\left(\zeta\frac{w}{2}\right)\cdot x_s}{\zeta^2 w} \\ &+8\frac{\cos\left(\zeta\frac{z_s}{2}\right)\sin\left(\zeta\frac{w}{2}\right)}{\zeta^3 w}\end{aligned} \tag{20b}$$

$$\begin{aligned}\frac{1}{N}\mathcal{S}_{\text{conc}}(\xi,0) = &-4\frac{\cos\left(\xi\frac{x_s}{2}\right)\cos\left(\xi\frac{w}{2}\right)}{\xi^2} + 4\frac{\sin\left(\xi\frac{x_s}{2}\right)\sin\left(\xi\frac{w}{2}\right)\cdot z_s}{\xi^2 w} \\ &+8\frac{\cos\left(\xi\frac{x_s}{2}\right)\sin\left(\xi\frac{w}{2}\right)}{\xi^3 w}\end{aligned} \tag{20c}$$

$$\frac{1}{N}\mathcal{S}_{\text{conc}}(0,0) = x_s\cdot z_s + \frac{w^2}{3}. \tag{20d}$$

The functions $S_{\text{swept}}\cdot\underline{I}$ or $S_{\text{conc}}\cdot\underline{I}$ are are inserted in place of $\mathcal{J}_z/\mathrm{i}\xi$ inside the equations (11a) to give the complete B-field solution.

Both the swept and the concentric coil models produce similar results for the speed sensor prototype analyzed in this paper. However, the results presented in the rest of this paper are obtained using the concentric coil model since it has a higher degree of symmetry, which may be beneficial for applications with in-plane speed measurement ($v_x \neq 0$ and $v_z \neq 0$).

F. VOLTAGE CALCULATION

The final outputs of the model are the terminal voltages of all three coils, from which the sensor's sensitivity / linearity and energy consumption due to the eddy-current losses in the mover (excluding the Joule losses in the injection coil and the losses in the yoke) can be assessed, based on the voltages of the pick-up coils and the injection coil, respectively. Each coil voltage results as the derivative of the corresponding flux linkage:

$$u(t) = \frac{\mathrm{d}\Psi}{\mathrm{d}t}, \tag{21}$$

which is the sum of the flux linked by each turn

$$\Psi = \Phi_{\text{turn 1}} + \Phi_{\text{turn 2}} + \cdots + \Phi_{\text{turn}N}. \tag{22}$$

Each of these flux linkages is obtained by integrating the normal component of the flux density field B_y over the area inside the wire turn. Instead of these individual integrals, the total flux linkage can be expressed as

$$\Psi = \int_{-\infty}^{\infty}\int_{-\infty}^{\infty} B_{y(x,z)} \cdot \underbrace{S_{\text{out}(x,z)}}_{\text{“}N(x,z)\text{”}}\,\mathrm{d}x\,\mathrm{d}z. \tag{23}$$

The already used *linkage function* $S(x, y)$ – this time for the output coil – gives the number of turns that contain the point x, z, which determines how many flux summands $\Phi_{\text{turn}\,n}$ include the B_y field at x, z. S thus becomes a "mask" or weighting factor under the integral.

To solve the integral in the Fourier domain, we utilize the convolution property

$$\begin{aligned}&F(\xi,\zeta)\cdot G(\xi,\zeta) \text{ corresponds to } (f*g)(x,z) \\ &= \int_{-\infty}^{\infty}\int_{-\infty}^{\infty} f(\tilde{x},\tilde{z})\cdot g(x-\tilde{x},z-\tilde{z})\,\mathrm{d}\tilde{x}\,\mathrm{d}\tilde{z}.\end{aligned} \tag{24}$$

Evaluating the inverse transform at $[x, z] = [0, 0]$, we find

$$\begin{aligned}&\frac{1}{(2\pi)^2}\int_{-\infty}^{\infty}\int_{-\infty}^{\infty} F(\xi,\zeta)\cdot G(\xi,\zeta)\cdot \mathrm{e}^0\,\mathrm{d}\xi\,\mathrm{d}\zeta \\ &= \int_{-\infty}^{\infty}\int_{-\infty}^{\infty} f(\tilde{x},\tilde{z})\cdot g(-\tilde{x},-\tilde{z})\,\mathrm{d}\tilde{x}\,\mathrm{d}\tilde{z}.\end{aligned} \tag{25}$$

This result is equivalent to the Parseval / Plancherel theorem, from which complex conjugation in $f\cdot\overline{g}$ and $F\cdot\overline{G}$ has been removed by appropriately taking negative arguments.

Defining $g(-x,-z) := S_{\text{out}}(x,z)$ such that $G(\xi,\zeta) = \mathcal{S}_{\text{out}}(-\xi,-\zeta)$, we have for the flux linkage phasor $\underline{\Psi}$

$$\underline{\Psi} = \frac{1}{(2\pi)^2}\int_{-\infty}^{\infty}\int_{-\infty}^{\infty} \mathcal{B}_y(\xi,c,\zeta)\cdot\mathcal{S}_{\text{out}}(-\xi,-\zeta)\,\mathrm{d}\xi\,\mathrm{d}\zeta. \tag{26}$$

To further clarify the mathematical relations, we rewrite $\mathcal{B}_y$ by introducing a *transmission factor* $\mathcal{T}$

$$\mathcal{B}_y =: \mathcal{T}\cdot(\mathcal{J}_z/\mathrm{i}\xi) = \mathcal{T}_{(\xi,\zeta)}\cdot\mathcal{S}_{\text{in}(\xi,\zeta)}\cdot\underline{I} \tag{27}$$

$$\mathcal{T}_{(\xi,\zeta)} = \alpha\left[\frac{C_n}{\mathcal{J}_z/\mathrm{i}\xi}\right]\mathrm{e}^{\alpha c} - \alpha\left[\frac{D_n}{\mathcal{J}_z/\mathrm{i}\xi}\right]\mathrm{e}^{-\alpha c}. \tag{28}$$

C_n, D_n are chosen as C_2, D_2 for pick-up coils placed above injection coils ($y > d$), or C_3, D_3 for pick-up coils placed below injection coils ($y < d$).

In the frequently used case where the injection and pick-up coils at the same height, either coefficient pair may be taken, and the transmission factor has a particularly simple expression:

$$\mathcal{T} = \frac{\alpha\cdot\boldsymbol{mre}\cdot\boldsymbol{comm}\cdot\mu_0}{2\cdot\boldsymbol{denom}}. \tag{29}$$

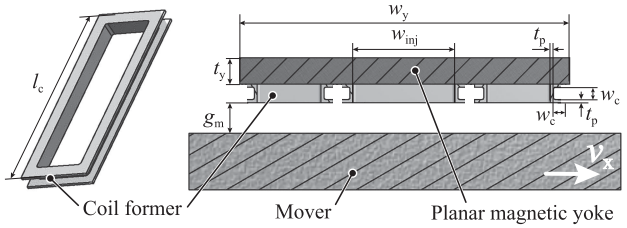

FIGURE 8. Parametric definition of the sensor geometry. The coils, which are not shown, are wound directly in the slots of the 3-D printed plastic coil formers.

TABLE 1. Parameters of the Speed Sensor Hardware Prototype

Symbol	Description	Value
w_{inj}	Injection and pick-up coil width	15 mm
N_{inj}	Injection coil winding turns	70
$N_{pick\text{-}up}$	Pick-up coil winding turns	200[1]
R_{inj}	Injection coil DC resistance	3.8 Ω
L_{inj}	Injection coil inductance (200 Hz, $d \to \infty$)	485 μH
w_y	Yoke width	64 mm
t_y	Yoke thickness	5.1 mm
t_p	Coil former wall thickness	0.6 mm
w_c	Coil side width	2.4 mm
l_c	Coil length	50 mm
	Yoke material	Ferrite N87
	Mover material	Aluminum Ac-112

With $\frac{\mathrm{d}}{\mathrm{d}t} \mathrel{\widehat{=}} \mathrm{i}\omega$ for phasors, the coil voltages are given by:

$$\underline{U} = \frac{\mathrm{i}\omega}{(2\pi)^2} \int_{-\infty}^{\infty} \int_{-\infty}^{\infty} \underline{I} \cdot \mathcal{S}_{\mathrm{in}} \cdot \mathcal{T} \cdot \mathcal{S}_{\mathrm{out}}^{-} \, \mathrm{d}\xi \, \mathrm{d}\zeta \tag{30a}$$

$$\mathcal{S}_{\mathrm{in}} := \mathcal{S}_{\mathrm{base}}[x_{s.\mathrm{in}}, z_{s.\mathrm{in}}, w_{\mathrm{in}}] \, \mathrm{e}^{-\mathrm{i}\xi \, x_{c.\mathrm{in}} - \mathrm{i}\zeta \, z_{c.\mathrm{in}}} \tag{30b}$$

$$\mathcal{S}_{\mathrm{out}}^{-} := \underbrace{\mathcal{S}_{\mathrm{base}}}_{\mathcal{S}_{\mathrm{conc}} \text{ or } \mathcal{S}_{\mathrm{swept}} \text{ or } \mathcal{S}_{\mathrm{fil}}} [x_{s.\mathrm{out}}, z_{s.\mathrm{out}}, w_{\mathrm{out}}] \, \mathrm{e}^{\mathrm{i}\xi x_{c.\mathrm{out}} + \mathrm{i}\zeta z_{c.\mathrm{out}}} \tag{30c}$$

Although $\mathcal{S}_{\mathrm{out}}^{-}$ represents $\mathcal{S}_{\mathrm{out}}(-\xi, -\zeta)$, inverting ξ and ζ in $\mathcal{S}_{\mathrm{base}}$ itself is not required due to the point symmetry of all discussed linkage functions.

For the voltage on the injection coil, which may be evaluated for calculating the self-inductance or the eddy-current losses in the mover, the formula is used with identical input and output coils ($x_{s.\mathrm{in}} = x_{s.\mathrm{out}}$ etc.). Difference voltages are easily calculated by setting $\mathcal{S}_{\mathrm{out}}^{-} = \mathcal{S}_{\mathrm{out},1}^{-} - \mathcal{S}_{\mathrm{out},2}^{-}$. Setups with more than one injection coil could be modeled using a superposition of multiple $\underline{I} \cdot \mathcal{S}_{\mathrm{in}}$ terms.

III. MODEL RESULTS

The model developed so far is used in this section for calculating the eddy current distribution in the mover for a few selected operating conditions. Fig. 8 and Table 1 define the sensor prototype considered in this analysis. For all the results presented in the following, the injected current is $i_{\mathrm{inj,RMS}} = 250$ mA, injection angular frequency is $\omega = 2\,\pi\,200$ rad/s, and the mechanical air gap is $g_{\mathrm{m}} = 8$ mm. Since the model assumes the injection and pick-up coils to be only two-dimensional, their vertical position is set to $d = g_{\mathrm{m}} + t_{\mathrm{p}} + w_{\mathrm{c}}/2$ in the models. For the sake of simplicity,

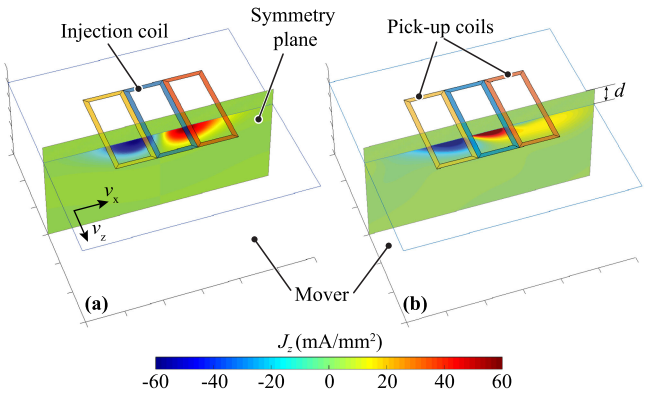

FIGURE 9. Induced eddy current density J_z inside the mover at standstill (a); and at a speed of $v_x = 12$ m/s (b). The injected current is of the form $i_{inj} = 250\sqrt{2}\,\mathrm{mA_{RMS}}\cos(\omega t)$, and $\omega = 2\,\pi\,200$ rad/s. The J_z distribution is plotted for the $\omega t = 0$ rad instant and $d = 11.6$mm.

the constant current source energizing the injection coil is assembled with a constant-amplitude ac voltage source and a large series resistor. In a practical application, where a current controller is used, the control must have sufficient bandwidth to reject any disturbance, e.g. coming from different induced voltages in the injection coil at different speeds.

In the model, a linear magnetic yoke with infinite height is assumed. In practical sensor realizations, where the yoke thickness is finite, the model is valid if the yoke is not saturated. As typically for this type of sensor, the flux densities in the yoke are very low and far from saturation (cf. [9]), the yoke thickness is chosen such that it is mechanically stable, and the model is valid since the yoke is not saturated.

Fig. 9(a) and Fig. 9(b) depict the z-component of the induced eddy currents J_{z} inside the mover at standstill and at a speed of $v_{\mathrm{x}} = 12$ m/s, respectively. It is clearly visible that the current distribution is symmetrical around the injection coil at standstill, and sheared in the axis of movement when the mover is in motion. This, in turn, leads to a difference in voltages induced in the pick-up coils, which constitutes the fundamental operating principle of this speed sensor.

The induced current density J is shown on the mover's top surface for standstill in Fig. 10(a), for a one-dimensional movement ($v_x = 12$m/s, $v_z = 0$) in Fig. 10(b), and for an in-plane movement ($v_x = v_z = 12$m/s) in Fig. 10(c). Again, a shearing of the induced current density distribution is visible in the direction of motion. This implies that, by adding pick-up coils on both sides of the injection coil also in the z-direction, a speed sensor that can measure the speed in both directions can be designed. The advantage of the analytic model is that motion in z-direction (cf. Fig. 10(c)) can be analyzed, where this would not be possible with 2D FEM. In addition, solving the proposed analytic model takes a few seconds, whereas solving 2D FEM takes several minutes.

IV. EXPERIMENTAL VERIFICATION

The speed sensor hardware prototype and the complete test bench used for the verification of the analytical models is

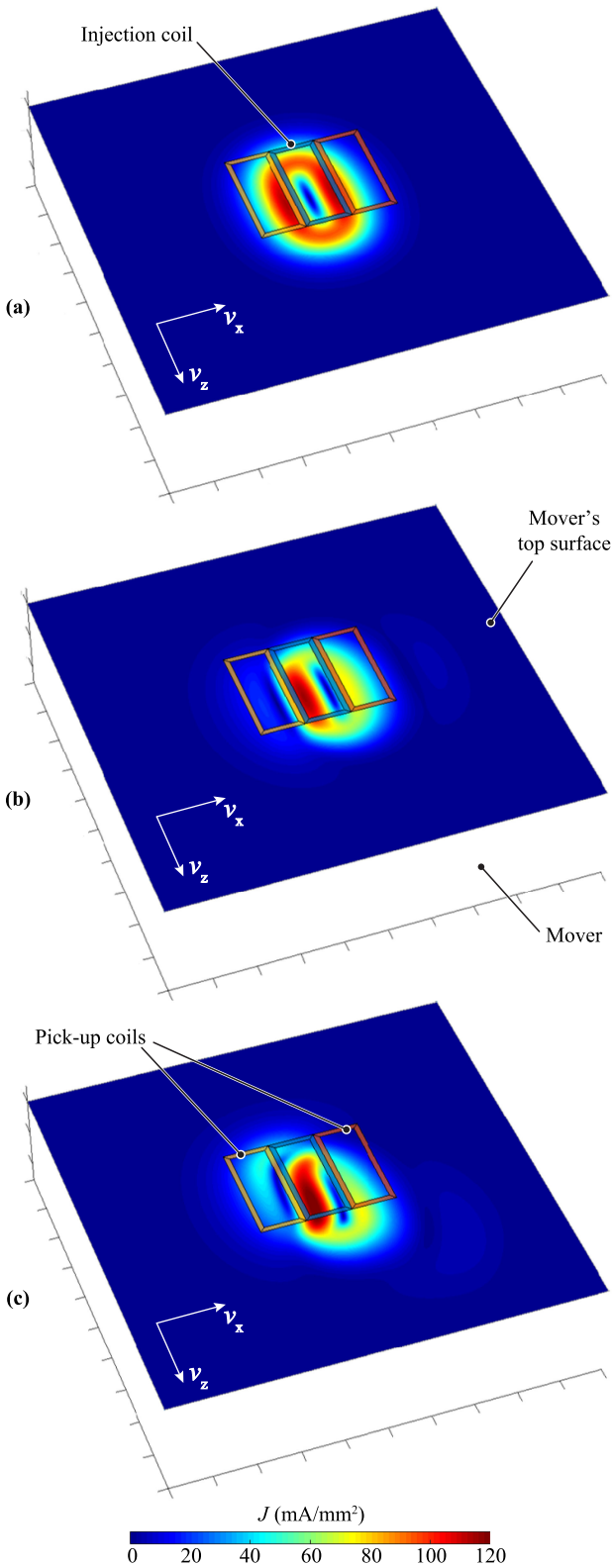

FIGURE 10. Induced eddy current density J on the top surface of the mover, for standstill (a); for a one-dimensional movement ($v_x = 12$m/s, $v_z = 0$) (b); and for an in-plane movement ($v_x = v_z = 12$m/s) (c). The injected current is of the form $i_{inj} = \sqrt{2}\,250\,\text{mA}_{RMS}\cos(\omega t)$, and $\omega = 2\,\pi\,200$ rad/s. The J distribution is plotted for $\omega t = 0.5\,\pi$ rad (a), $\omega t = 1.3\,\pi$ rad (b), and $\omega t = 0.24\,\pi$ rad (c) instants. The coils are positioned at $d = 11.6$mm.

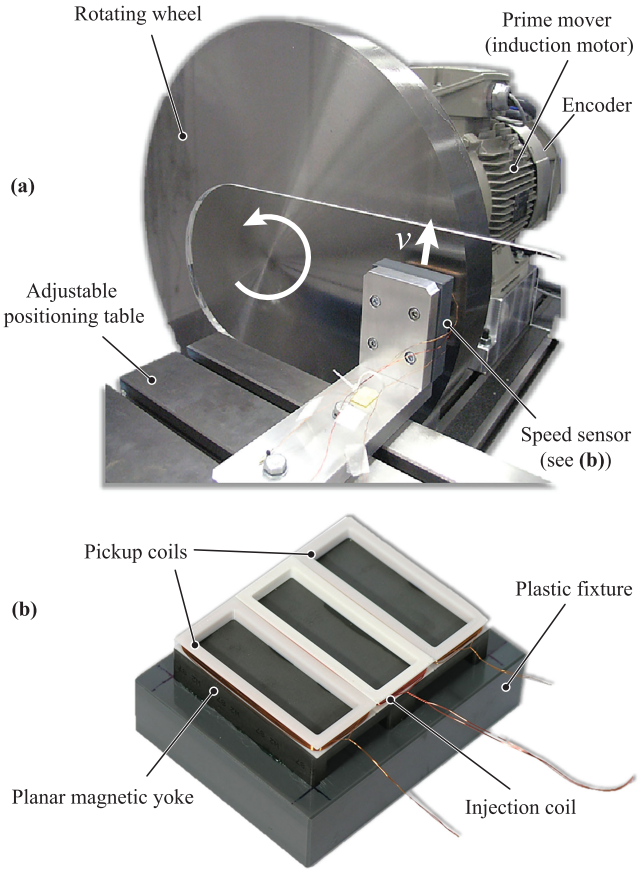

FIGURE 11. Speed sensor prototype (a), and the complete test bench (b) that are presented in [9], and used for the experimental validation of the analytical models developed in this paper.

depicted in Fig. 11. The design parameters of the sensor prototype are summarized in Table 1. Since the detailed description of the sensor design and the test bench operation can be found in [9], they are omitted here for the sake of brevity; and analytical models developed in this paper are verified in the following by means of comparison to the experimental results published in [9]. Since the model assumes the injection and pick-up coils to be only two-dimensional, their vertical position is set to $d = g_m + t_p + w_c/2$ in the model.

Fig. 12 shows the comparison of the model and the measurement results for an injection angular frequency of $\omega = 2\,\pi\,200$ rad/s, a mechanical air gap of $g_m = 8$ mm and a speed range of $v_x = [3...12]$ m/s. The injected current zero-crossing instant coincidences with the 0 s time instant in all the figures; hence, it is to be noted that not only the amplitude, but also the phase of the measured voltage u_{diff} depends on the speed of the mover. Nevertheless, the dependency of the amplitude on the speed is much more significant than that of the phase.

Fig. 13 compares the amplitudes of the measured voltage, $\hat{u}_{diff}$, obtained by the analytical model and from measurements for mechanical air gaps of $g_m = [8, 12]$ mm, injection frequencies of $\omega = [100, 200, 300, 400]\,2\pi$ rad/s and a speed range of $v_x = [3...12]$ m/s. It can be seen that a very good

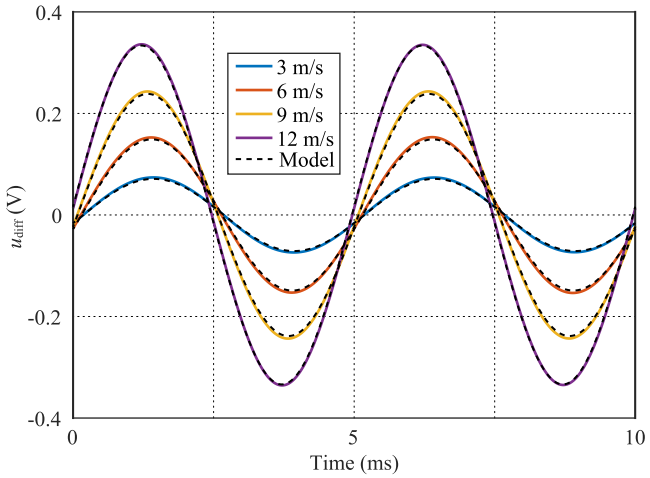

FIGURE 12. Comparison of the results of the presented model and measurement results from [9] for a mechanical air gap of $g_m = 8$ mm, an injection angular frequency of $\omega = 200\,2\pi$, an injected current of $i_{inj} = 250\ mA_{RMS}$, and a speed range of $v_x = [3...12]$ m/s. The parameters of the sensor are given in Table 1.

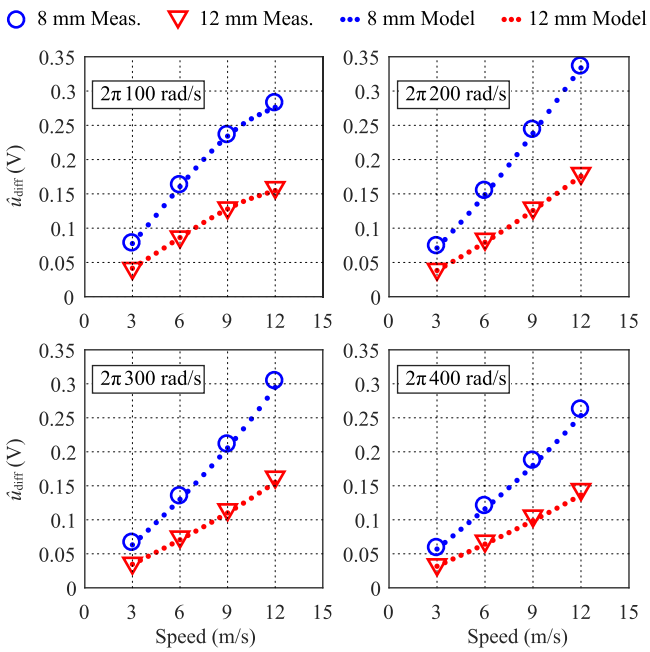

FIGURE 13. Comparison of the results of the presented model and measurement results from [9] for an injected current of $i_{inj} = 250\ mA_{RMS}$, mechanical air gaps of $g_m = [8, 12]$ mm, injection frequencies of $\omega = [100, 200, 300, 400]\,2\pi$ rad/s and a speed range of $v_x = [3...12]$ m/s. The parameters of the sensor are given in Table 1. Dashed lines represent model results and measurement points are denoted with circles and triangles in solid lines.

match exists for a wide range of operating conditions. It should be seen that the sensor optimum operation frequency is around 200 Hz, since it results in the highest $\hat{u}_{diff}$. Too low frequency (e.g. 100 Hz) does not induce enough voltage in the pick-up coils, whereas too high frequency (e.g. 400 Hz) loads to skin effect in the mover. The optimum frequency would look different for different mover materials and sensor geometries.

V. CONCLUSION

Eddy-current-based, non-contact speed sensors have been presented in literature for the challenging task of sensing the speed of smooth surfaces in harsh operating conditions, without mechanical contact. Several scholars have dealt with the computationally efficient modeling of such sensors. This paper contributes to the field by presenting an analytical model that is able to model a sensor featuring a magnetic yoke, which increases the sensor's signal-to-noise ratio and/or decreases its power consumption by intensifying the air gap flux density for the same injected current. Moreover, a yoke shields the sensor magnetically and avoids a potential magnetic interference of the sensor with its environment. The presented model assumes an infinite horizontal size of the magnetic yoke, which is verified with the prototype presented in the paper.

Unlike the common path taken in existing literature, the modeling is not based on the superposition of incident and reflected fields. Instead, the injected current is accounted for in the boundary conditions. Special attention is given to the modeling of the in-plane spreading of the coils by deriving coil-shape functions. Maxwell's equations are solved directly for the magnetic flux density vector, and the study of a higher-order vector potential is omitted. The magnetic field and eddy current distributions in the whole problem space are obtained by algebraically solving a 12-by-12 linear equation system.

The results of the model are visualized in the form of eddy current distributions in the mover, for different operating conditions. Finally, validity of the model is confirmed by comparing it to the experimental results published earlier.

Even though a hardware demonstrator is shown, the focus of the paper is on the analytical modeling. Further discussion of practical realization and FEM modeling can be found in [9].

Future work will focus on the model verification for different operating points and its improvements in case of remaining discrepancies with measurements.

ACKNOWLEDGMENT

The authors would like to express their sincere appreciation to Nabtesco Corp., Japan, for technical support of research on non-contact speed sensing. In particular, inspiring technical discussions with K. Nakamura, Y. Tsukada and Y. Ono are acknowledged.

REFERENCES

[1] E. Cardelli, A. Faba, and F. Tissi, "Contact-less speed probe based on eddy currents," *IEEE Trans. Magn.*, vol. 49, no. 7, pp. 3897–3900, Jul. 2013.

[2] M. Poloujadoff, B. Morel, and A. Bolopion, "Simultaneous consideration of finite length and finite width of linear induction motors," *IEEE Trans. Power App. Syst.*, no. 3, pp. 1172–1180, May 1980.

[3] S. Paul, "Three-dimensional steady state and transient eddy current modeling," Ph.D. dissertation, Elect. Comput. Eng. Dept., The University of North Carolina at Charlotte, 2014.

[4] N. Takehira, A. Tanaka, and K. Toda, "Analysis of a speed meter utilizing eddy current effect," *Elect. Eng. Jpn.*, vol. 97, no. 5, pp. 1–8, Sep. 1977, translated from Denki Gakkai Ronbunshi, vol. 97 A, no. 9, pp. 457–464, Sep. 1977.

[5] N. Takehira and A. Tanaka, "Analysis of transmission-type speedometer utilizing eddy current effect," *Elect. Eng. Jpn.*, vol. 100, no. 5, pp. 1–7, Sep. 1980, translated from Denki Gakkai Ronbunshi, vol. 100 A, no. 9, pp. 483–490, Sep. 1980.
[6] A. Tanaka, N. Takehira, and K. Toda, "Analysis of a rectangular coil facing a moving sheet conductor," *Elect. Eng. Jpn.*, vol. 101, no. 4, pp. 15–22, Aug. 1981, translated from Denki Gakkai Ronbunshi, vol. 101 A, no. 8, pp. 405–412, Aug. 1981.
[7] A. Tanaka and N. Takehira, "Eddy current speed meter using galvanomagnetic devices," *Elect. Eng. Jpn.*, vol. 106, no. 4, pp. 29–36, Jun. 1986, translated from Denki Gakkai Ronbunshi, vol. 106 A, no. 4, pp. 267–274, Jun. 1986.
[8] M. Mirzaei and P. Ripka, "A linear eddy current speed sensor with a perpendicular coils configuration," *IEEE Trans. Veh. Technol.*, vol. 70, no. 4, pp. 3197–3207, Apr. 2021.
[9] A. Tüysüz, M. Flankl, J. W. Kolar, and A. Mütze, "Eddy-current-based contactless speed sensing of conductive surfaces," in *Proc. 2nd IEEE Annu. Southern Power Electron. Conf.*, 2016, pp. 1–6.
[10] M. Mirzaei, J. Machac, P. Ripka, A. Chirtsov, J. Vyhnanek, and V. Grim, "Design of a flat-type magnetic position sensor using a finite-difference method," *IET Science, Meas. Technol.*, vol. 14, no. 5, pp. 514–524, 2020.
[11] V. Bandaru, I. Sokolov, and T. Boeck, "Lorentz force transient response at finite magnetic reynolds numbers," *IEEE Trans. Magn.*, vol. 52, no. 8, pp. 1–11, Aug. 2016.
[12] Z. Liu, W. Li, F. Xue, J. Xiafang, B. Bu, and Z. Yi, "Electromagnetic tomography rail defect inspection," *IEEE Trans. Magn.*, vol. 51, no. 10, pp. 1–7, Oct. 2015.
[13] K. Sakai, K. Morita, Y. Haga, T. Kiwa, K. Inoue, and K. Tsukada, "Automatic scanning system for back-side defect of steel structure using magnetic flux leakage method," *IEEE Trans. Magn.*, vol. 51, no. 11, pp. 1–3, Nov. 2015.
[14] S. Nagata and M. Numachi, "Eddy current non-destructive evaluation for healthiness of radiator structure," *IEEE Trans. Magn.*, vol. 53, no. 11, pp. 1–4, Nov. 2017.
[15] H. E. Knoepfel, *Magnetic Fields: A Comprehensive Theoretical Treatise for Practical Use*. Wiley, 2008.
[16] N. Takehira and A. Tanaka, "Analysis of a perpendicular-type eddy-current speed meter," *Phys. Sci., Meas. Instrum., Manage. Educ. - Rev., IEE Proc. A*, vol. 135, no. 2, pp. 89–94, Feb. 1988.
[17] N. Paudel, "Dynamic suspension modeling of an eddy-current device: An application to MAGLEV," Ph.D. dissertation, Elect. Comput. Eng. Dept., The Univ. North Carolina at Charlotte, 2012.
[18] T. Itaya, K. Ishida, A. Tanaka, N. Takehira, and T. Miki, "Eddy current distribution for a rectangular coil arranged parallel to a moving conductor slab," *Sci., Meas. Technol., IET*, vol. 6, no. 2, pp. 43–51, Mar. 2012.
[19] T. Itaya, K. Ishida, A. Tanaka, and N. Takehira, "Analysis of a fork-shaped rectangular coil facing moving sheet conductors," *Sci., Meas. Technol., IET*, vol. 3, no. 4, pp. 279–285, Jul. 2009.

ARDA TÜYSÜZ received the B.Sc. degree in electrical engineering from Istanbul Technical University, Istanbul, Turkey, in 2006, the M.Sc. degree in electrical power engineering from RWTH Aachen University, Aachen, Germany, in 2009, and the Ph.D. degree in electrical drives from the Swiss Federal Institute of Technology (ETH) Zurich, Zurich, Switzerland, in 2015.

Between 2015 and 2017, he was a Postdoctoral Researcher with Power Electronic Systems Laboratory, ETH Zurich. He is currently with ABB Corporate Research Center, Ladenburg, Germany. His research interests include novel electrical machine topologies, self-sensing control of high-speed electrical machines, and wide-bandgap power devices for very efficient and compact electrical drive systems.

TIBOR STOLZ studied electrical engineering with the Swiss Federal Institute of Technology (ETH) Zurich, Zurich, Switzerland, focusing on power electronics, electric drives, and renewable energy. In the master's thesis, he developed analytical eddy current models for various applications in mechatronics, including a graphical user interface for easy access to the simulations.

Since June 2017, he has been with the Power Electronic Systems Laboratory, ETH Zurich, extending this project as a Scientific Assistant.

ANNETTE MUETZE (Fellow, IEEE) received the Dipl.-Ing. degree in electrical engineering from the Darmstadt University of Technology, Darmstadt, Germany, in 1999, the Diploma in general engineering from the Ecole Centrale de Lyon, Ecully, France, in 1999, and the Dr.-Ing. degree in electrical engineering from the Darmstadt University of Technology in 2004.

She is a currently Full Professor with the Graz University of Technology, Graz, Austria, where she heads the Electric Drives and Machines Institute and the Christian Doppler Laboratory for Brushless Drives for Pump and Fan Applications. Prior to joining the Graz University of Technology, she was an Assistant Professor with the Department of Electrical and Computer Engineering, University of Wisconsin, Madison, WI, USA, and an Associate Professor with the School of Engineering, University of Warwick, Coventry, U.K.

Dr. Muetze was the recipient of the NSF CAREER Award in 2004.

MICHAEL FLANKL (Student Member, IEEE) received the B.Sc. degree in mechatronics from JKU Linz, Linz, Austria, in 2012 and the M.Sc. degree in robotics, systems and control from ETH Zurich, Zurich, Switzerland, in 2014.

Since May 2014, he has been working toward the Ph.D. degree with Power Electronic Systems Laboratory, ETH Zurich. He is supervised by Prof. Johann W. Kolar and working on mechatronic energy harvesting solutions. His further areas of interests include electric transportation and drive systems.

SPASOJE MIRIĆ (Student Member, IEEE) received the B.Sc., M.Sc., and Ph.D. degrees in electrical engineering from the University of Belgrade, Belgrade, Serbia, in 2012, 2013, and 2018 respectively, and the second Ph.D. degree in 2021 in electrical engineering from the Swiss Federal Institute of Technology (ETH) Zurich, Zurich, Switzerland, focusing on novel electrical machine topologies, linear machines and bearingless motors for highly dynamic actuator systems. He is currently a Postdoctoral Researcher with ETH Zurich focusing on modern drive systems with wide-band gap power semiconductors and multilevel power electronic converters.

JOHANN W. KOLAR (Fellow, IEEE) received the M.Sc. and Ph.D. degree (summa cum laude/promotio sub auspiciis praesidentis rei publicae) from the Vienna University of Technology, Vienna, Austria, in 1997 and 1999, respectively. Since 1984, he has been an Independent Researcher and International Consultant in close collaboration with the Vienna University of Technology, in the fields of power electronics, industrial electronics and high performance drive systems. He is currently a Full Professor and the Head of the Power Electronic Systems Laboratory, Swiss Federal Institute of Technology (ETH) Zurich, Zurich, Switzerland. He has proposed numerous novel PWM converter topologies, modulation and control concepts, and multi-objective power electronics design procedures, and has supervised more than 70 Ph.D. students. He has authored or coauthored more than 900 scientific papers in international journals and conference proceedings, four book chapters, and has filed more than 190 patents. His current research interests include ultra-compact and ultra-efficient SiC and GaN converter systems, ANN-based power electronics components and systems design, solid-state transformers, power supplies on chip, and ultra-high speed and ultra-light weight drives, bearingless motors, and energy harvesting. He has presented more than 30 educational seminars at leading international conferences, was with IEEE PELS Distinguished Lecturer from 2012 to 2016, and was the recipient of 34 IEEE transactions and conference Prize Paper awards, the 2014 IEEE Power Electronics Society R. David Middlebrook Achievement Award, the 2016 IEEE William E. Newell Power Electronics Award, the 2016 IEEE PEMC Council Award, and two ETH Zurich Golden Owl Awards for excellence in teaching. He has initiated and/or is the Founder of four ETH Spin-off companies.